Advanced Energy Conversion Materials
http://ojs.wiserpub.com/index.php/AECM/

UNIVERSAL WISER PUBLISHER

Research Article

Evaporated Chalcopyrite Thin Films for Indoor Photovoltaic Applications

Cecilia Guillén

Research Centre for Energy, Environment and Technology, Complutense Avenue 40, 28040 Madrid, Spain
Email: c.guillen@ciemat.es

Received: 31 October 2023; **Revised:** 20 November 2023; **Accepted:** 27 November 2023

Abstract: The feasibility of capturing indoor artificial light using chalcopyrite photovoltaic absorbers has been analyzed. For this purpose, various chalcopyrite compounds ($CuInSe_2$, $CuInS_2$ and $CuGaS_2$) were prepared by evaporation and then measured to obtain their main structural, morphological and optical characteristics. On the other hand, several artificial light sources were selected (incandescent, halogen, fluorescent, high-pressure sodium, metal halide and LED lamps) and represented by their respective spectral radiance. The absorption characteristics of $CuInSe_2$ and $CuInS_2$ are optimal for collecting light from fluorescent lamps and warm or cool white LEDs, requiring only a small film thickness of about 0.6 μm to capture 90-100% of the light radiance. Otherwise, the efficiency of $CuGaS_2$ is found to increase as the color temperature of the LED lamp increases, being always lower and more dependent on the film thickness than for the other evaporated compounds. The worst performances (collection of less than 50% of the light radiance) correspond to incandescent and halogen lamps, which have a significant emission in the infrared region outside the absorption range of the evaporated chalcopyrite films. These results provide guidelines for the design of chalcopyrite-based photovoltaic devices suitable for operation under different indoor lighting conditions.

***Keywords*:** chalcopyrite thin films, $CuInSe_2$, $CuInS_2$, $CuGaS_2$, artificial light sources, indoor photovoltaic applications

1. Introduction

The development of materials for the use of optical energy ranges from photoelectrocatalysts [1] to photothermal [2] and photovoltaic applications [3]. More specifically, there is great growth in photovoltaic systems and telecommunication devices. Recent studies linking both fields show that indoor energy harvesting by suitable photovoltaic cells can help implement concepts such as the internet of things for smart homes and smart cities [3-4]. Indoor photovoltaic cells make it possible to power electronic devices from local light sources and can also be used as optical data receivers in the context of visible light communications [5-6].

Various photovoltaic materials have achieved great development, including crystalline silicon (c-Si), amorphous silicon (a-Si), cadmium telluride (CdTe) and copper indium gallium selenide ($CuIn_{1-x}Ga_xSe_2$ or CIGS), which now share the market for outdoor applications [7]. $CuIn_{1-x}Ga_xSe_2$ belongs to the I-III-VI_2 semiconductor alloys with a chalcopyrite structure, presenting the advantage of an adjustable bandgap between 1.0 eV ($CuInSe_2$) and 1.7 eV ($CuGaSe_2$) to achieve high photovoltaic conversion efficiency [8]. Another chalcopyrite alloy is $CuIn_{1-x}Ga_xSe_2$, with an adjustable bandgap between 1.5 eV ($CuInS_2$) and 2.4 eV ($CuGaS_2$) [9]. These chalcopyrite materials are commonly prepared as thin films on

DOI: https://doi.org/10.37256/aecm.5120243853

different substrates [9-10] since due to their high absorption coefficient (~ 10^4 cm^{-1}) a low thickness (~ 1 μm) is required to absorb the radiation energy greater than the bandgap [8]. In fact, new designs are being developed to minimize the thickness below 0.5 μm, which saves material and manufacturing time [10]. On the other hand, it is worth highlighting the excellent stability and negligible toxicity of ternary chalcopyrites, which have been tested both in photovoltaic devices [11] and in biosensors for phototherapy [12].

Chalcopyrite thin films have been well developed to collect energy from outdoor solar radiation [13]. However, estimating its indoor performance is complicated because there is no universally accepted standard for indoor spectral quality and integrated irradiance (analogous to the standard AM1.5 G solar spectrum) [3, 14]. There are many artificial light sources, which have been grouped into three categories [15]: 1) incandescent and halogen lamps, whose spectrum corresponds to a blackbody radiator at 2,800 K, 2) fluorescent lamps, with a correlated color temperature that changes between 2,000 K and 6,000 K depending on the composition of the internal gas, and 3) high-pressure sodium, metal halide and LED lamps, which also have different color temperatures depending on their composition. LED lamps deserve special interest because they significantly reduce the energy consumption for lighting and are considered the most environmentally friendly among all artificial light sources [16]. At this point, it should be noted that there are white LEDs with different spectral characteristics according to their color temperature, which affects the amount of energy captured by a given indoor photovoltaic converter [17].

For the present work, the optical absorption coefficients of various chalcopyrite thin films ($CuInSe_2$, $CuInS_2$ and $CuGaS_2$ grown by evaporation) were measured and analyzed to test their feasibility for harvesting radiation from several artificial light sources (belonging to the three categories and with different color temperatures), which are represented by their respective spectral radiance. The percentage of energy collected is calculated based on the thickness of the absorber film for the various combinations of light sources and chalcopyrite materials. The objective is to contribute to the design of photovoltaic devices with chalcopyrite absorbers suitable for operation under different indoor lighting conditions, adding the possibility of reducing material consumption according to the minimum absorber thickness required in each case.

2. Materials and methods

Thin films of $CuInSe_2$, $CuInS_2$ and $CuGaS_2$ were prepared by modulated flux deposition in a custom-designed vacuum chamber [18]. It contains a rotating holder that transports soda-lime glass substrates at 30 rpm around for evaporation from Cu, In, and Ga beam sources, heating to 350 ºC by halogen lamps, and reaction with vapor from elemental Se or S sources in every rotation. Before use, the substrates were degreased with neutral soap, rinsed with deionized water, and dried in air. The base pressure was 10^{-6} mbar and the evaporation time was about 20 min to obtain a film thickness t = 0.6 μm, which was verified by post-deposition measurements with a Dektak 3,030 profilometer.

The films were examined by X-Ray Diffraction (XRD) in a Philips X'pert instrument, with radiation CuKα (λ = 1.54056 Å) and a Bragg-Brentano θ-2θ configuration. The tetragonal chalcopyrite structure was identified regarding the standard Powder Diffraction Files (PDF) for the different compounds. The mean crystallite size (S) was calculated from the Full Width at Half Maximum (FWHM = β) of the main diffraction peak located at the Bragg reflection angle θ, applying the Scherrer formula [19]: $S = 0.94\ \lambda/(\beta \cos\theta)$. The topography was examined by Atomic Force Microscopy (AFM) with a Park XE-100, taking digital images that allow surface roughness to be quantified. The optical characterization was based on transmittance (T) and reflectance (R) data recorded with a double beam spectrophotometer Perkin-Elmer Lambda 9 in the wavelength range λ = 300-1,800 nm. The transmittance is corrected for reflection losses, T_c (%) = 100 T (%)/(100-R (%)), and the optical absorption coefficient is calculated as [20]: $\alpha = (1/t)$ ln [100/T_c (%)], including the film thickness value (t).

In order to evaluate the performance of chalcopyrite absorbers under typical indoor conditions, several commercial light sources (incandescent, halogen, fluorescent, high-pressure sodium, metal halide and LED lamps) have been considered in this work. They were selected to cover a wide range of illumination intensities and color temperatures, as well as different spectral radiances [21], which were obtained from the National Oceanic and Atmospheric Administration (NOAA) database [22].

3. Results and discussion

All the evaporated films show a tetragonal chalcopyrite structure, according to the XRD patterns depicted in Figure 1(a). The diffraction peaks are indexed regarding the standard PDF cards for $CuInSe_2$ (card No. 40-1487), $CuInS_2$ (card No. 27-0159), or $CuGaS_2$ (card No. 25-0279), and no secondary phases are observed. In these chalcopyrite structures, each anion (Se^{2-} or S^{2-}) is tetrahedrally coordinated to two Cu^+ cations and two In^{3+} or Ga^{3+} cations, while each cation (Cu^+ and In^{3+} or Ga^{3+}) is surrounded by four anions (Se^{2-} or S^{2-}) [23]. The largest lattice parameters correspond to $CuInSe_2$, decreasing by the substitution of Se by S in $CuInS_2$ and furthermore by the substitution of In by Ga in $CuGaS_2$ [24]. Lower lattice parameters explain the shift of the diffraction peaks toward higher diffraction angles. The (112) reflection is predominant in these compounds, as has been explained by the availability of the chalcopyrite structure for massive surface reconstruction [25]. This is due to the low defect formation energies on the cationic sublattice, which make the polar {112} planes more stable than the non-polar {110} surfaces in tetrahedra [26]. A detailed analysis of the (112) diffraction peak is also presented in Figure 1(b), including the mean crystallite size (S_{112}) calculated from the FWHM for each sample [19]. The crystallite size is somewhat higher in the evaporated $CuInSe_2$ (S_{112} = 47 nm) than in $CuInS_2$ (S_{112} = 38 nm) and $CuGaS_2$ (S_{112} = 37 nm) layers, which may be related to the fact that the substitution of Se by *S* increases the compound formation heat [27]. The substrate temperature (set at 350 °C) is high enough to achieve chalcopyrite formation in all cases, but provides a greater scope for crystallization of $CuInSe_2$ compared to $CuInS_2$ and $CuGaS_2$.

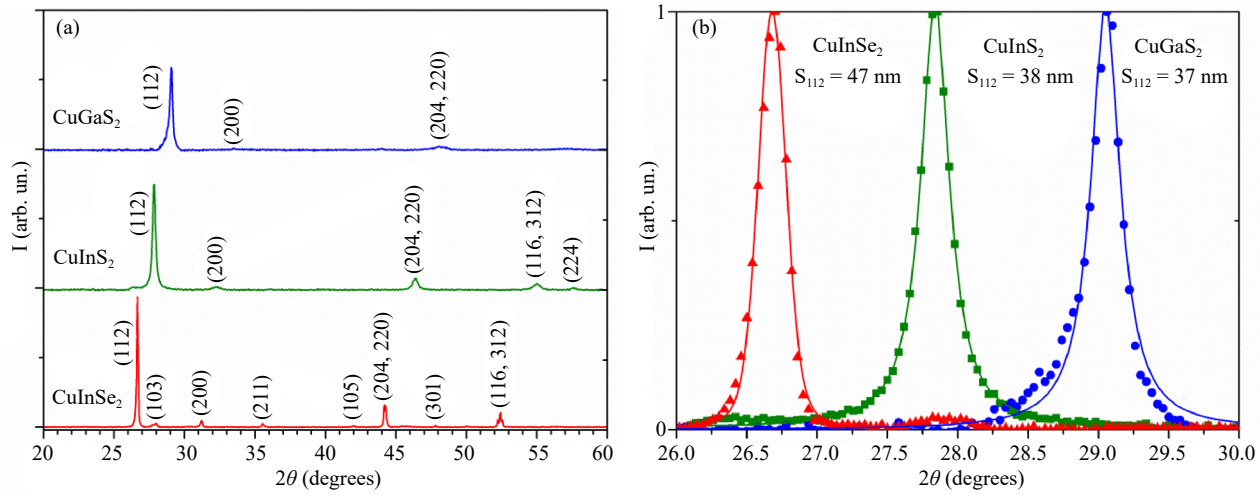

Figure 1. (a): XRD patterns, and (b): detail of the main (112) reflection for the evaporated $CuInSe_2$, $CuInS_2$ and $CuGaS_2$ thin films. The mean crystallite size obtained from the (112) peak width (S_{112}) is included

The surface morphology and the corresponding root-mean-square roughness (R_q), as analyzed by AFM for the various samples, are presented in Figure 2(a). The evaporated layers are constituted by small grains grouped in cauliflower-like clusters that are typical of chalcopyrite thin films [28]. The surface roughness (R_q ~ 60 nm) is suitable for efficient photovoltaic cells [29], with no significant differences for the various compounds. This is because all depositions were carried out under the same temperature and pressure conditions. In other cases, it has been observed that the surface roughness increases when the heating temperature [28] and/or the base pressure [30] increases, due to the coalescence and reorganization of the grains. Figure 2(b) shows the scan lines taken by profilometry for the respective layers, where the film thickness (*t*) is given by the height from the chalcopyrite surface (where the scan starts) to the glass substrate (where the measurement ends).

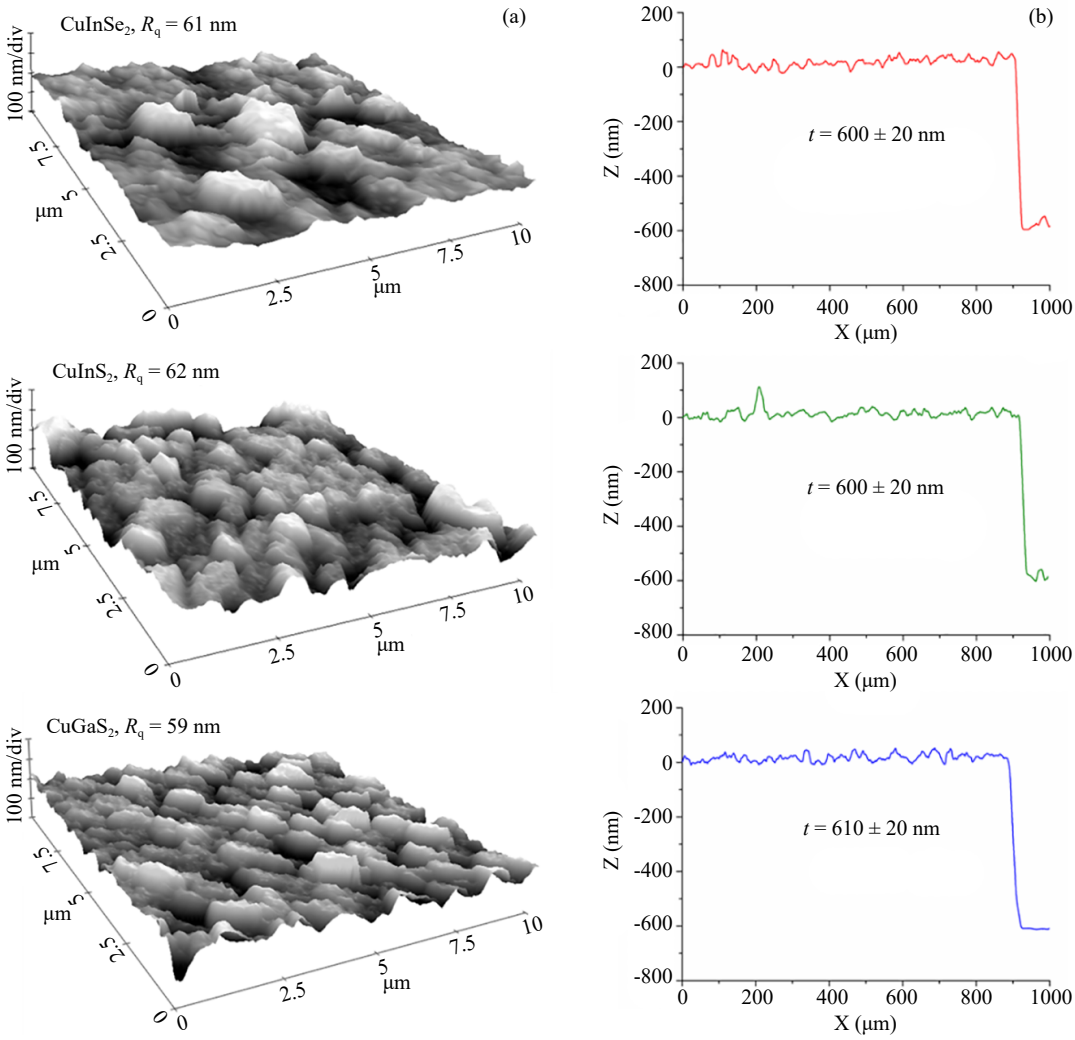

Figure 2. (a): AFM images taken on 10 µm × 10 µm areas, and (b): Profilometric measurements on 1,000 µm lines for the various chalcopyrite layers. The root-mean-square roughness (R_q) and the film thickness (t) are included for each sample

Figure 3(a) contains the optical transmittance and Figure 3(b) the corresponding absorption spectra for the different chalcopyrite layers. All the films show high absorption within the visible spectral range, especially at wavelengths $\lambda <$ 600 nm or energies $E >$ 2.07 eV, as required for their application in outdoor photovoltaics. Compared to $CuGaS_2$, the absorption extend towards the near-infrared for $CuInS_2$ and further for $CuInSe_2$, due to the difference in bandgap energy (E_g) for each material [31]. In the high absorption region ($\alpha > 10^4$ cm^{-1}) the experimental data show a good fit to the expression $\alpha_1 = A\,(E - E_g)^{1/2}$, which is typical of direct transitions [20], giving the E_g values specified in Table 1. It is known that in $CuInSe_2$ the valence band maximum (VBM) consists of Cu 3d and Se 4p orbitals, while the conduction band minimum (CBM) consists of In 5s and Se 4p orbitals [24]. Therefore, substituting the anion Se by S is expected to change both VBM and CBM in $CuInS_2$ with respect to $CuInSe_2$, but substituting In by Ga changes only the CBM but not the VBM in $CuGaS_2$ with respect to $CuInS_2$. The forbidden bandwidth is the energy difference between CBM and VBM, which is observed at 1.02 eV for $CuInSe_2$ [32], and higher for $CuInS_2$ and $CuGaS_2$ according to the literature [33-34].

During gap calculations, the presence of some absorption below E_g has been considered, which is due to tail states that are typical of chalcopyrite materials [35]. In this region ($E < E_g$) the absorption coefficient has been fitted to the form [36]: $\alpha_2 \propto \exp\{-(E - E_t)^2/2\sigma^2\}$, where E_t is a characteristic transition energy and σ represents the width of the tail [37]. The density of states has a point of inflection from the expected decay below the conduction band edge (below

E_g) to the increase due to the tail of the band (located at E_t), and the measured absorption may appear almost linear at energies between E_g and E_t [38]. Table 1 includes the results of the fits illustrated in Figure 3(b) for the various samples, being in the same order as reported for analogous photovoltaic absorbers [39]. It should be noted that band tails depend on the presence of defects and structural disorders in these compounds [40]. Therefore, the optical absorption coefficients in Figure 3(b) include information about the structural and morphological features shown in Figures 1 and 2.

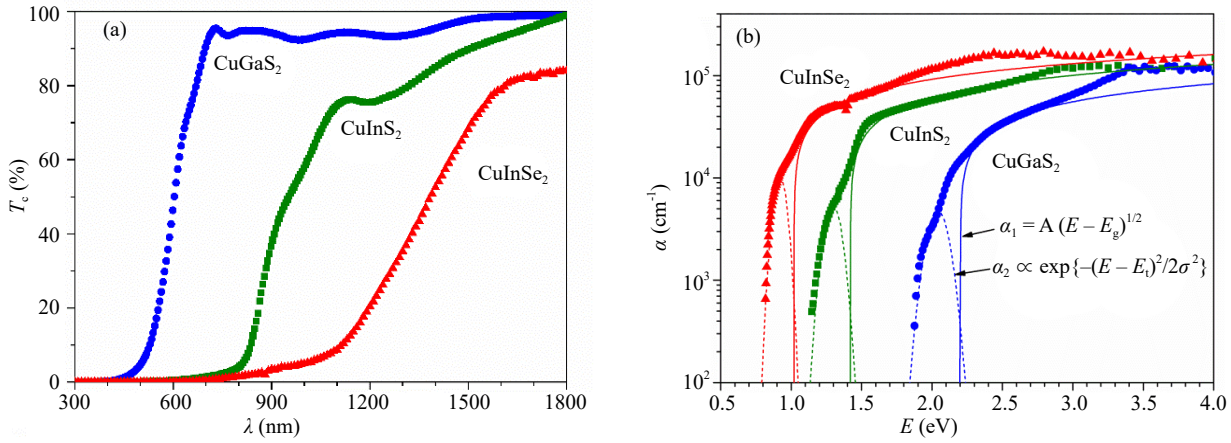

Figure 3. (a): Optical transmittance (T_c), and (b): Absorption coefficient (α) data obtained as a function of the radiation wavelength (λ) or energy (E) for the diverse chalcopyrite layers

Table 1. Summary of the main characteristics of evaporated chalcopyrite thin films, including the mean crystallite size (S_{112}), root-mean-square roughness (R_q), gap energy (E_g) and band tail width (σ)

Sample	S_{112} (nm)	R_q (nm)	E_g (eV)	σ (eV)
$CuInSe_2$	47	61	1.02	0.042
$CuInS_2$	38	62	1.42	0.057
$CuGaS_2$	37	59	2.20	0.071

The optical absorption coefficients achieved for these chalcopyrite films have been used to evaluate their performance under different indoor illuminations. For this purpose, the spectral radiances of typical artificial light sources (incandescent, halogen, fluorescent, high-pressure sodium, metal halide and LED lamps obtained from the NOAA database [22]) are plotted in Figure 4. Specifically, the first group in Figure 4(a) includes various light sources with a similar Correlated Color Temperature (CCT = 2,000-2,800 K) [21], but different illumination intensities (R_i = 5-58 W/m^2) calculated by integration of the respective radiance spectrum. Another group in Figure 4(b) contains only LED lamps, which deserve particular attention due to their large commercial growth, and are shown for different CCT ranging from 2,038 K (warm glow) to 7,419 K (cool white). It is important to note that all the LED spectra have a blue emission peak located at $\lambda_1 \sim 450$ nm in addition to the main emission at $\lambda_2 \sim 600$ nm, and the color temperature increases with the ratio between both maxima (I_1/I_2) [17]. Otherwise, the illumination intensity value is independent of the color temperature, as it is illustrated in Figure 4(b).

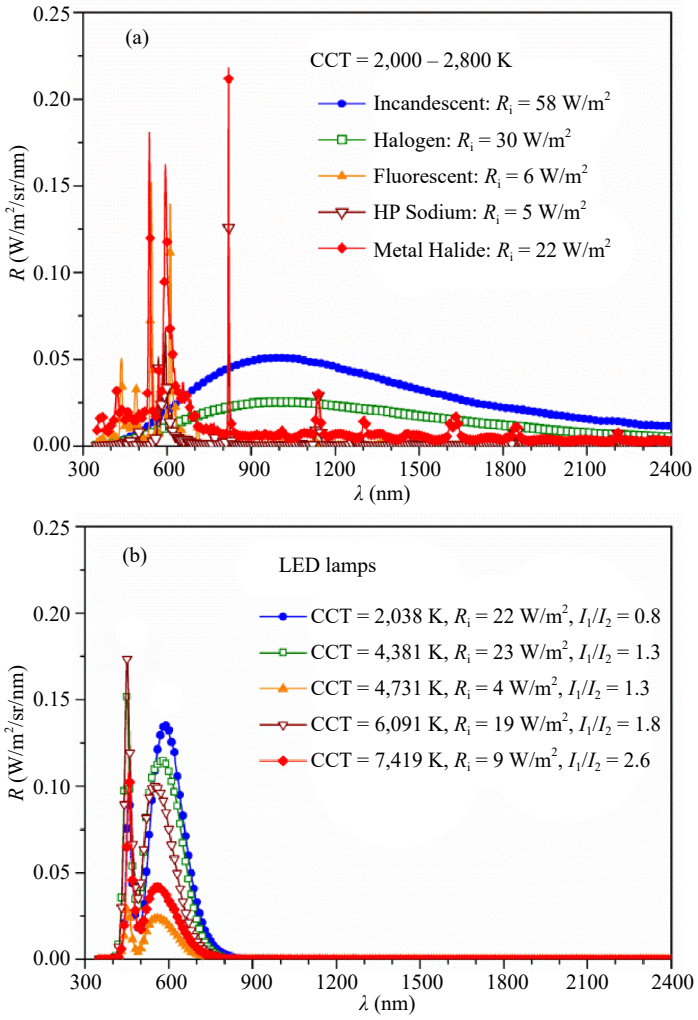

Figure 4. (a): Radiance of artificial light sources with similar Correlated Color Temperature (CCT), and (b): Radiance of LED lamps with different CCTs, including the integrated value (R_i) obtained for each one. In the case of LED lamps, the ratio of the two emissions (I_1/I_2) is also included

For each of the light sources, the illumination intensity that can be absorbed by one of the chalcopyrite films is given by the product of the lamp radiance (R) and the chalcopyrite absorptance at each wavelength [41]: $A = 1 - e^{-\alpha(\lambda)t}$, which depends on the absorption coefficient (α) and the film thickness (t). In this way, the percentage of radiance that is adsorbed, $P = (R \times A)/R_i$, has been calculated from the previous data (Figures 3 and 4) and it is represented in Figure 5 as a function of the absorber thickness for the various combinations of light sources and chalcopyrite materials. The lowest values ($P < 50\%$) correspond to the incandescent and halogen lamps, in Figure 5(a), which have a significant radiance in the infrared region requiring absorbers with a low bandgap energy ($E_g < 1.0$ eV). Obviously, the light collection is better when the lamps have lower infrared emissions. Thus, the use of a thin $CuInSe_2$ film ($t \sim 0.6$ μm) allows obtaining $P = 70\%$ in the case of high-pressure sodium or metal-halide emissions, while both $CuInSe_2$ and $CuInS_2$ layers with $t \sim 0.6$ μm are suitable to achieve $P = 90\%$ in the case of fluorescent lamp. The same percentage ($P = 90\%$) is obtained in Figure 5(b) with a lower thickness of $CuInS_2$ ($t = 0.35$ μm) or $CuInSe_2$ ($t = 0.25$ μm) for all the LED lamps, achieving $P \sim 100\%$ when $t \sim 0.6$ μm. Otherwise, the efficiency of $CuGaS_2$ is found highly dependent on the film thickness and the color temperature of the LED, being for the thickest layer ($t \sim 1.0$ μm) in the range $P = 70$-85%, increasing as the color temperature increases. Previous studies on the indoor conversion efficiency of different photovoltaic absorbers have indicated that warm white LEDs are preferred for material bandgaps of 1.5 eV or less, and cool white LEDs for higher bandgap compounds [17]. However, the results in Figure 5(b) show that both warm and cool white LEDs are optimal for absorbers with $E_g \leq 1.5$ eV, and cool white LEDs are better for higher bandgap materials.

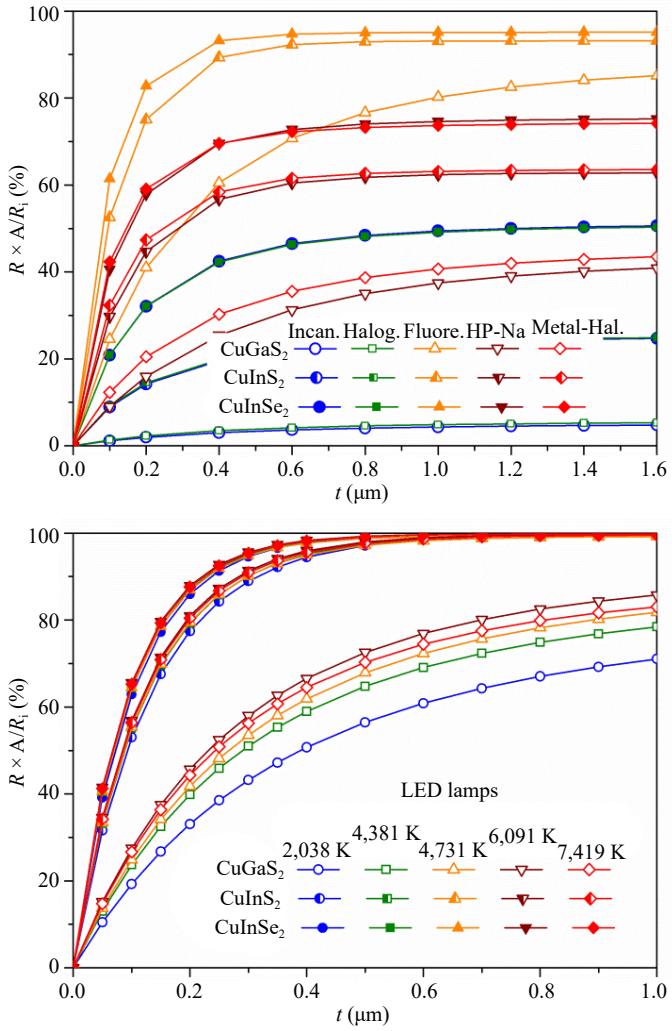

Figure 5. (a): Percentage of the lamps radiance in Figure 4(a), and (b): Percentage of the LEDs radiance in Figure 4(b) that is absorbed by the chalcopyrite films as a function of their thickness

4. Conclusions

All the evaporated films have tetragonal chalcopyrite structure with predominant (112) orientation, smooth surfaces (roughness $R_q \sim 60$ nm) and high optical absorption within the visible region ($\alpha > 10^4$ cm^{-1} at $\lambda < 600$ nm). The absorption extends towards the near-infrared when the bandgap energy decreases from $E_g = 2.20$ eV for $CuGaS_2$ to $E_g = 1.42$ eV for $CuInS_2$ and $E_g = 1.02$ eV for $CuInSe_2$. Some additional absorption is detected below E_g due to band tails, which have a width that increases in the range $\sigma = 42$-71 meV as the gap energy increases.

Comparing artificial light sources with a similar correlated color temperature (CCT = 2,000-2,800 K), the infrared radiance is high for incandescent and halogen lamps, lower for high-pressure sodium or metal-halide emissions and minimum in the case of fluorescent and LED lamps. White LEDs with different color temperatures (from warm glow with CCT = 2,038 K to cool white with CCT = 7,419 K) all show a main emission around 600 nm wavelength and a blue emission at 450 nm, increasing the color temperature with the blue emission ratio.

The percentage of radiance that can be absorbed by $CuInSe_2$ is around 50% for incandescent and halogen lamps and around 70% for high-pressure sodium or metal-halide emissions. Furthermore, both $CuInSe_2$ and $CuInS_2$ films can collect 90% of the fluorescent radiance and 100% of LED emissions (for all CCT values), requiring only a small thickness of about 0.6 μm. Otherwise, $CuGaS_2$ with 1.0 μm thickness can capture 80% of the fluorescent emission and of cool white LEDs (with CCT ≥ 4,731 K), although its efficiency decreases when the color temperature of the LED

light decreases.

Conflict of interest

The author declares no competing financial interest.

References

[1] Tong T, Zhang M, Chen W, Huo X, Xu F, Yan H, et al. Recent advances in carbon-based material/semiconductor composite photoelectrocatalysts: Synthesis, improvement strategy, and organic pollutant removal. *Coordination Chemistry Reviews*. 2024; 500: 215498.

[2] Hu S, Qin L, Yi H, Lai C, Yang Y, Li B, et al. Carbonaceous materials-based photothermal process in water treatment: From originals to frontier applications. *Small*. 2023; 2305579. Available from: doi.org: 10.1002/smll.20230557.

[3] Pecunia V, Silva SRP, Phillips JD, Artegiani E, Romeo A, Shim H, et al. Roadmap on energy harvesting materials. *Journal of Physics: Materials*. 2023; 27: 1-31.

[4] Mathews I, Kantareddy SN, Buonassisi T, Peters IM. Technology and market perspective for indoor photovoltaic cells. *Joule*. 2019; 3: 1415-1426.

[5] Bouclé J, Ribeiro Dos Santos D, Julien-Vergonjanne A. Doing more with ambient light: Harvesting indoor energy and data using emerging solar cells. *Solar*. 2023; 3(1): 161-183.

[6] Patel M, Bhatnagar P, Lee J, Kumar N, Nguyen TT, Kim J. Transparent photovoltaic window for visible light communications with onsite power and reliable machine learning features. *Nano Energy*. 2023; 115: 108696.

[7] Chee AKW. On current technology for light absorber materials used in highly efficient industrial solar cells. *Renewable and Sustainable Energy Reviews*. 2023; 173: 113027.

[8] Liu W, Li H, Qiao B, Zhao S, Xu Z, Song D. Highly efficient CIGS solar cells based on a new CIGS bandgap gradient design characterized by numerical simulation. *Journal of Solar Energy*. 2022; 233: 337-344.

[9] Kim S, Nagai T, Tampo H, Ishizuka S, Shibata H. Large open-circuit voltage boosting of pure sulfide chalcopyrite $Cu(In,Ga)S_2$ prepared using Cu-deficient metal precursors. *Progress in Photovoltaics Research and Applications*. 2020; 28(8): 816-822.

[10] Shin MJ, Lee A, Park JH, Cho A, Ahn SK, Shin D, et al. Ultrathin $Cu(In,Ga)Se_2$ transparent photovoltaics: An alternative to conventional solar energy-harvesting windows. *Nano Energy*. 2022; 92: 106711.

[11] Rockett AA. Current status and opportunities in chalcopyrite solar cells. *Current Opinion in Solid State and Materials Science*. 2010; 14(6): 143-148.

[12] Girma WM, Fahmi MZ, Permadi A, Abate MA, Chang JY. Synthetic strategies and biomedical applications of I-III-VI ternary quantum dots. *Journal of Materials Chemistry B*. 2017; 5(31): 6193-6216.

[13] Meddeb H, Götz-Köhler M, Neugebohrn N, Banik U, Osterthun N, Sergeev O, et al. Tunable photovoltaics: Adapting solar cell technologies to versatile applications. *Advanced Energy Materials*. 2022; 12(28): 2200713.

[14] Li M, Igbari F, Wang Z, Liao L. Indoor thin-film photovoltaics: Progress and challenges. *Advanced Energy Materials*. 2020; 10(28): 2000641.

[15] Minnaert B, Veelaert P. A proposal for typical artificial light sources for the characterization of indoor photovoltaic applications. *Energies*. 2014; 7(3): 1500-1516.

[16] Jarosz G, Marczyński R, Signerski R. Effect of band gap on power conversion efficiency of single-junction semiconductor photovoltaic cells under white light phosphor-based LED illumination. *Materials Science in Semiconductor Processing*. 2020; 107: 104812.

[17] Saha A, Haque KA, Baten MZ. Performance evaluation of single-junction indoor photovoltaic devices for different absorber bandgaps under spectrally varying white Light-Emitting Diodes. *IEEE Journal of Photovoltaics.* 2020; 10(2): 539-545.

[18] Guillén C, Herrero J. $CuInS_2$ and $CuGaS_2$ thin films grown by modulated flux deposition with various Cu contents. *Physica Status Solidi (A)-Applications and Materials Science*. 2006; 203(10): 2438-2443.

[19] Vorokh AS. Scherrer formula: Estimation of error in determining small nanoparticle size. *Nanosystems: Physics, Chemistry, Mathematics*. 2018; 9(3): 364-369.

[20] Woods-Robinson R, Han Y, Zhang H, Ablekim T, Khan I, Persson KA, et al. Wide band gap chalcogenide

semiconductors. *Journal of Chemical Reviews*. 2020; 120(9): 4007-4055.
[21] Elvidge CD, Keith DM, Tuttle BT, Baugh KE. Spectral identification of lighting type and character. *Sensors*. 2010; 10(4): 3961-3988.
[22] Earth Observation Group. *National oceanic and atmospheric administration-laboratory spectra*. 2023. Available from: https://ngdc.noaa.gov/eog/night_sat/spectra.html [Accessed 19 June 2023].
[23] Coughlan C, Ibáñez M, Dobrozhan O, Singh A, Cabot A, Ryan KM. Compound copper chalcogenide nanocrystals. *Journal of Chemical Reviews*. 2017; 117(9): 5865-6109.
[24] Wada T. Materials science of chalcopyrite-type and multinary solar cells compounds: Crystal structure and electronic structure of CISe, CZTS, CTS and the related compounds. *The Japanese Journal of Applied Physics*. 2022; 220204(2022): 1-9.
[25] Siebentritt S, Papathanasiou N, Albert J, Lux-Steiner MC. Stability of surfaces in the chalcopyrite system. *Applied Physics Letters.* 2006; 88(15): 2006-2008.
[26] Jaffe J, Zunger A. Defect-induced nonpolar-to-polar transition at the surface of chalcopyrite semiconductors. *Physical Review Applied B.* 2001; 64(24): 241304.
[27] Tang K, Künecke U, Oehlschläger F, Hölzing A, Schurr R, Hock R, et al. Differential calorimetry study of the initial stage of the sulphurisation process of $CuInSe_2$ solar cell materials. *Solar Energy Materials and Solar Cells*. 2010; 94(11): 1875-1879.
[28] Ullah S, Mollar M, Marí B. Electrodeposition of $CuGaSe_2$ and $CuGaS_2$ thin films for photovoltaic applications. *Journal of Solid State Electrochemistry*. 2016; 20: 2251-2257.
[29] Jiang J, Giridharagopal R, Jedlicka E, Sun K, Yu S, Wu S, et al. Highly efficient copper-rich chalcopyrite solar cells from DMF molecular solution. *Nano Energy*. 2020; 69: 104438.
[30] Sharmin A, Bashar MS, Sultana M, Al Mamun SMM. Sputtered single-phase kesterite Cu_2ZnSnS_4 (CZTS) thin film for photovoltaic applications: Post annealing parameter optimization and property analysis. *AIP Advances*. 2020; 10(1): 15230.
[31] Kim ST, Yoo JS, Lee MW, Jung JW, Jang JH. $CuInSe_2$-based near-infrared photodetector. *Applied Sciences*. 2021; 12(1): 92.
[32] Yadav J, Singh M. Effect of heat treatment temperature on preparation and characterization of $CuInSe_2$ thin films. *Journal of Materials Science: Materials in Electronics*. 2023; 34(8): 692.
[33] Bangolla HK, Nallapureddy RR, Santhosh Kumar MC. Cu-rich copper indium sulfide thin films deposited by co-evaporation for photovoltaic applications. *Journal of Materials Science: Materials in Electronics*. 2023; 34: 341.
[34] Wang L, Yuan X, Wang Y, Yao W, Zhu J, Jing W. Preparation and characterization of $CuGaS_2$ thin films as a promising parent material for intermediate band solar cells. *Materials Science in Semiconductor Processing*. 2015; 30: 267-270.
[35] Nishiwaki M, Nagaya K, Kato M, Fujimoto S, Tampo H, Miyadera T, et al. Tail state formation in solar cell materials: First principles analyses of zincblende, chalcopyrite, kesterite, and hybrid perovskite crystals. *Physical Review Materials*. 2018; 2(8): 1-28.
[36] Katahara JK, Hillhouse HW. Quasi-Fermi level splitting and sub-bandgap absorptivity from semiconductor photoluminescence. *Journal of Applied Physics*. 2014; 116(17): 173504.
[37] Sritrakool W, Sa-yakanit V, Glyde HR. Band tails in disordered systems. *Physical Review B*. 1986; 33(2): 1199-1202.
[38] Mieghem PV. Theory of band tails in heavily doped semiconductors. *Reviews of Modern Physics*. 1992; 64(3): 755-792.
[39] Rey G, Larramona G, Bourdais S, Choné C, Delatouche B, Jacob A, et al. On the origin of band-tails in kesterite. *Solar Energy Materials and Solar Cells*. 2018; 179: 142-151.
[40] Wasim SM, Marín G, Marquez R, Rincón C. On the effect of structural disorders on the Urbach's tails of ternary chalcopyrite semiconductors and related ordered defect compounds. *Journal of Applied Physics*. 2020; 127(3): 35703.
[41] Massiot I, Cattoni A, Collin S. Progress and prospects for ultrathin solar cells. *Nature energy*. 2020; 5: 959-972.